Materials Science & Engineering A 965 (2026) 150303

Contents lists available at ScienceDirect

Materials Science & Engineering A

journal homepage: www.elsevier.com/locate/msea

Precipitation behavior and anisotropic creep deformation behavior of laser powder bed fusion processed Hastelloy X at 1173 K

Tomotaka Hatakeyama [*], Kota Sawada, Masahiro Kusano, Makoto Watanabe

Research Center for Structural Materials, National Institute for Materials Science, 1-2-1, Sengen, Tsukuba, Ibaraki, 305-0047, Japan

ARTICLE INFO

Keywords:
Laser powder bed fusion
Hastelloy X
Creep
Precipitation
Grain boundary

ABSTRACT

Hastelloy X was fabricated using Laser Powder Bed Fusion (LPBF). Creep tests of the as-built samples were conducted at 1173 K under conditions in which the build direction was parallel or perpendicular to the stress axis. The creep rupture time for samples with the stress axis parallel to the build direction was comparable to that of conventionally manufactured Hastelloy X. However, for samples with the stress axis perpendicular to the build direction, the creep rupture time was shorter by one order of magnitude. To elucidate the cause of this anisotropy, the microstructure of the creep-ruptured samples was analyzed using scanning electron microscopy-electron backscatter diffraction (SEM-EBSD). Precipitates were classified using EBSD pattern matching, successfully and more efficiently revealing the precipitation sites of four types of precipitates compared to traditional methods such as SEM-energy dispersive spectroscopy (SEM-EDS) and transmission electron microscopy-selected area diffraction pattern (TEM-SADP) analysis. The specific precipitates did not influence the formation of creep voids and cracks. Crack propagation occurred at high-angle grain boundaries, which were preferentially aligned parallel to the build direction and exhibited a significant deviation in the Taylor factor between adjacent grains. The anisotropy in the creep strength was attributed to the distribution of high-angle grain boundaries formed during the LPBF process, as these boundaries facilitated crack propagation when the stress axis was perpendicular to the build direction.

1. Introduction

Laser powder bed fusion (LPBF) is an additive manufacturing technique that enables the fabrication of complex geometries and achieves rapid solidification, resulting in unique microstructural development [1] and improved material properties [2]. Despite its advantages, there is a lack of comprehensive creep data for LPBF-processed materials, including those tested for thousands of hours, highlighting the need for further investigation into their long-term creep behavior.

Hastelloy X is a solid-solution strengthened Ni-based alloy renowned for its excellent strength and oxidation resistance, making it suitable for high-temperature applications [3]. Extensive research has been conducted on LPBF-processed Hastelloy X, motivated by its high-temperature capabilities and favorable mechanical properties [4–12].

Sawada et al. conducted long-term creep tests of LPBF-processed Hastelloy X at temperatures ranging from 973 to 1273 K [13]. Their findings indicated that when the building direction was parallel to the stress direction, the creep strength was comparable to that of conventional Hastelloy X, whereas when the building direction was perpendicular to the stress direction, a significant reduction in the creep strength was observed. This anisotropic creep behavior is believed to be related to the differences in fracture morphology: zigzag cracks were observed when the building direction was parallel to the stress direction, whereas straight cracks were observed when it was perpendicular. However, the reasons for these different fracture morphologies have not been fully elucidated. To elucidate the origin of the anisotropic creep behavior, it is essential to characterize the microstructure of LPBF-processed Hastelloy X in detail.

One of the fucus of this study is the grain boundaries characterized by scanning electron microscopy-electron backscatter diffraction (SEM-EBSD) because the microstructural anisotropies in the LPBF-processed samples are featured by the grain boundary distribution owing to the elongated grains along the build direction.

Another focus of this study was the precipitation behavior during the creep exposure. Both conventionally processed and LPBF-processed Hastelloy X exhibited complex precipitation behavior during long-term exposure to elevated temperatures. Previous studies have

---

[*] Corresponding author.
E-mail address: hatakeyama.tomotaka@nims.go.jp (T. Hatakeyama).

https://doi.org/10.1016/j.msea.2026.150303
Received 17 February 2026; Received in revised form 14 April 2026; Accepted 21 April 2026

revealed the precipitation of Mo- and Cr-rich phases during creep at 1073 K [5]. Energy dispersive spectroscopy in an SEM (SEM-EDS) suggested that the Mo-rich phases were M_6C and μ phases, whereas the Cr-rich phases were $M_{23}C_6$ and σ phases. However, the evidence for this distinction remains insufficient, and the classification of these precipitates is challenging. Recently, topologically close packed (TCP) phases, such as the P and R phases, have been identified using selected area diffraction patterns (SADP) obtained by transmission electron microscopy (TEM) [12]. Owing to their similar chemical compositions, these precipitates cannot be distinguished by SEM-EDS; therefore, the relationship between the precipitation species and the macroscale microstructure remains unclear. Sawada et al. performed phase identification of precipitates in the grip portion of creep-ruptured specimens by X-ray diffraction (XRD) analysis of extracted residues, which detected $M_{23}C_6$, R, μ, and M_6C phases at 1173 K [13]. Although Cr-rich precipitates recognized in SEM-EDS were identified as $M_{23}C_6$, distinguishing between Mo-rich R, μ, and M_6C phases remains a challenge.

Table 1 summarizes the previously reported precipitates in wrought and LPBF-processed Hastelloy X [3,5,11–14]. The precipitation of two types of carbides ($M_{23}C_6$ and M_6C) and four types of intermetallic compounds (σ, μ, P, and R) was confirmed after exposure at 1073–1223 K. Their identification was based on SADP in TEM, chemical composition analyzed by SEM-EDS, or XRD of the extracted residue.

The advantages and disadvantages of these phase-identification techniques are summarized in Table 2. For example, SADP is suitable for structural analysis with geometrical information on the precipitation site in the microstructure. However, these analyses are restricted to small, localized regions. In addition, it may miss the spatial heterogeneity of precipitation behavior. Furthermore, sample preparation and manual acquisition of the SADP from each precipitate are costly. Nevertheless, understanding the spatial distribution of these precipitates is crucial for elucidating mechanical properties, particularly with respect to the anisotropy induced by the relationship between the building direction and stress direction. This underscores the necessity of an identification technique that distinguishes precipitate types and maps their distribution over a large area, which is impractical with TEM-based methods but feasible with SEM-based approaches.

Because EBSD pattern (EBSP) contains information on the crystal structure, this study applied phase identification methods using SEM-EBSD. Commercially available SEM-EBSD software automatically acquires the EBSP from a specified region at arbitrary intervals. These features are expected to overcome the disadvantages of phase identification methods using SADP, SEM-EDS, and XRD, as summarized in Table 2. Another advantage of using SEM-EBSD is that the EBSD data are also applicable to grain boundary characterization. However, the traditional indexing method of EBSP through Hough transformation [15,16] sometimes has difficulties when two or more phases with complex crystal structures are selected as candidates because of the duplication of the diffracted lattice planes.

Recently, "Spherical Indexing" was developed as a novel indexing procedure of EBSP, which uses the pattern matching of experimental EBSP and simulated EBSP [17,18]. Because Spherical Indexing uses entire patterns, an accurate classification of precipitates based on the differences in EBSPs is expected. In other words, as summarized in Table 2, the SEM-EBSD-based identification of precipitates combined with Spherical Indexing encompasses all the advantages of SADP, SEM-EDS, and XRD. Please note that the spatial resolution of EBSD is expected to be less than 100 nm [19], which is sufficient for the analysis of precipitates observed in the LPBF-processed Hastelloy X creep-ruptured at 1173 K [13].

Table 2
Comparison of identification methods for precipitates. Rating of the methods: excellent (***), good (**), poor (*), and impossible (–).

Methods[a]	SADP	EDS	XRD	SEM-EBSD
Structure analysis	***	-	***	**
Convenience	*	***	**	***
Statistical analysis	*	**	***	**
Geometrical information	***	***	-	***

[a] SADP: SADP in TEM, EDS: SEM-EDS, XRD: XRD of extracted residue.

In summary, although previous studies have identified several precipitate phases in LPBF-processed Hastelloy X, a clear distinction and spatial mapping of these precipitates at the macroscale remain insufficient. Nevertheless, understanding the contribution of each precipitate to the creep deformation behavior is important, as it has been reported that the coherent interface between the matrix and precipitate has high crack propagation arrestability [20], and the effective use of positive precipitates is expected by controlling the precipitation kinetics. To address this gap, we utilized a novel electron backscatter diffraction (EBSD) indexing method based on pattern matching with simulated master patterns (Spherical Indexing [17,18]). This enables the efficient and comprehensive identification and spatial mapping of precipitate types based on their crystal structures, in contrast to conventional TEM-based analyses. This approach will facilitate a greater understanding of precipitation behavior and anisotropy in LPBF-processed Hastelloy X. In addition, because SEM-EBSD mapping provides grain boundary information, we investigated and discussed the effect of the grain boundary misorientation angle on the precipitation and fracture behavior.

2. Experimental procedures

The chemical composition of the gas-atomized powder (Amperprint®0228.074, Höganäs AB) is listed in Table 3. The powder particle size ranged from 15 to 45 μm. Cylindrical specimens with a diameter of 15 mm and a length of 90 mm were manufactured by LPBF using an SLM

Table 3
Chemical composition of gas atomized powder (mass%).

Element	Cr	Fe	Mo	Co	W	C	Al	B
Powder	21.8	18.6	8.9	1.6	0.5	0.05	0.09	<0.002
Element	Mn	N	O	P	S	Si	Ti	
Powder	<0.0	0.006	0.018	<0.002	0.002	<0.1	<0.01	

Table 1
Review of precipitates observed in wrought and LPBF-processed Hastelloy X.

Reference	Process	Testing	Temperature (K)	Time (h)	Evidence[a]	Identified precipitates
Zhao et al. [14]	Wrought	Aging	1123	100	SADP	σ, $M_{23}C_6$, M_6C, μ
Zhao et al. [14]	Wrought	Aging	1173	100	SADP	σ, $M_{23}C_6$, M_6C, μ
Yoshioka et al. [3]	Wrought	Aging	1173	1000–10000	XRD	M_6C, μ
Agrawal et al. [5]	LPBF	Creep	1073	170	EDS	σ, $M_{23}C_6$, M_6C, μ
Agrawal et al. [11]	LPBF	Tensile	1173	-	EDS	$M_{23}C_6$, M_6C,
Agrawal et al. [12]	LPBF	Aging	1073	500	SADP	$M_{23}C_6$, μ
Agrawal et al. [12]	LPBF	Aging	1223	500	SADP	P, R
Sawada et al. [13]	LPBF	Aging	1173	5319.3	XRD	$M_{23}C_6$, R, μ, M_6C

[a] SADP: SADP in TEM, EDS: SEM-EDS, XRD: XRD of extracted residue.

280 3D printer (SLM solutions) under an argon flow. The processing parameters were a laser power of 300 W, scan speed of 909 mm/s, hatch distance of 0.1 mm, and layer thickness of 0.03 mm. A chessboard scan strategy with a 5 × 5 mm^2 square was employed. The laser scan direction was rotated by 90° in the neighboring squares and rotated by 67° at each layer.

The longitudinal direction of the cylinder was set as either parallel or perpendicular to the building direction to investigate the anisotropy of the creep strength. Specimens with parallel and perpendicular directions are referred to as PiHA and PiHC, respectively. The cylinders were machined into creep specimens with a gauge diameter of 6 mm and gauge length of 30 mm; the longitudinal direction of the cylinders was aligned with the stress direction. Creep tests were performed on the as-built specimens in air at 1173 K under constant loads of 60, 50, 40, and 30 MPa for PiHA and 50, 30, 20, and 15 MPa for PiHC [13] in accordance with JIS Z 2271 [21].

Both the as-built and gauge portion of creep-ruptured specimens that crept with time to rupture for several thousand hours at 1173 K—PiHA (30 MPa, tr = 5319.3 h) and PiHC (15 MPa, tr = 2949.5 h)—were sectioned along the longitudinal direction and embedded in the resin. The surfaces were carefully polished using SiC paper, diamond slurry, and colloidal silica for subsequent examination by scanning electron microscopy (SEM: Auriga Laser, ZEISS), electron backscattered diffraction (SEM-EBSD: Digiview, EDAX), and energy dispersive spectroscopy (SEM-EDS, Octane Super, EDAX). SEM observations were conducted at accelerating voltages of 5 or 15 kV. SEM-EDS and EBSD analyses were performed at 15 kV. All EBSD patterns (EBSPs) were saved and re-indexed using Spherical Indexing [17,18] with OIM Analysis 9 and OIM Matrix (EDAX).

3. Results and discussion

3.1. As-built microstructure and creep properties

Fig. 1(a) shows the inverse pole figure (IPF) map of the as-built PiHA with a step size of 1 μm. The normal direction of the sample surface is displayed in the IPF maps throughout this study. The building direction was from the bottom to the top of the images. A columnar grain structure elongated along the building direction was observed. This is a typical microstructure of LPBF-processed samples formed by the epitaxial growth along <001> direction [22,23]. Fig. 1(b) and (c) are IPF and kernel average misorientation (KAM) maps taken from the region indicated by the box in Fig. 1(a) with a step size of 200 nm. Minor misorientation in the grain interior was clearly visualized in the KAM map owing to the improved angular resolution by Spherical Indexing [24,25]. Fig. 1(d) and (e) are the SE image and Mo map obtained by SEM-EDS taken from the region indicated by the larger dashed boxes in Fig. 1(b) and (c). Parabolic lines with Mo depletion/enrichment were recognized in the microstructure, suggesting segregation at the melt pool boundaries. However, no precipitates were observed in the as-built samples. Fig. 1(f) shows the SE image taken from the region indicated by the smaller dashed boxes in Fig. 1(b)–(e). A submicron cellular structure was observed in the grain interior [26]. As indicated by the arrows, the longitudinal direction of the cellular structure changes at the melt pool boundary, even though the crystallographic orientation is preserved across the melt pool boundary (Fig. 1(b)) by epitaxial grain growth [27]. A comparison of Fig. 1(c) and (f) suggests that KAM is enhanced along the cell boundaries. Please note that the as-built PiHC has an identical microstructure to that of PiHA. No marked defects (e.g., pores, cracks) were observed in both as-built PiHA and PiHC.

Fig. 2(a) shows the relationship between the stress and time to rupture of PiHA and PiHC obtained at 1173 K. The data for the conventional Hastelloy X [28,29] are attached for comparison. The creep strength of PiHA was identical to the conventional Hastelloy X. In contrast, the creep strength of PiHC was significantly lower than that of the conventional Hastelloy X. Such anisotropic mechanical properties of LPBF-processed Hastelloy X at elevated temperatures have already been reported by shorter-term creep tests [5] or slow strain rate tensile testing [10]. Fig. 2(b) and (c) show the elongation and reduction of area of PiHA and PiHC as a function of time to rupture, respectively. The data for the conventional Hastelloy X [28,29] are attached for comparison. Fig. 2(b') and (c') are enlarged views of Fig. 2(b) and (c), respectively. They revealed that the creep rupture ductility of PiHA and PiHC are significantly lower than that of the conventional Hastelloy X. Nevertheless, no marked anisotropy on the creep rupture ductility was observed at 1173 K.

3.2. Precipitation behavior of creep-ruptured samples

Fig. 3 shows the crystal structure, space group, lattice parameter, and simulated spherical master patterns for the Ni matrix, $M_{23}C_6$, R, M_6C, and μ phases [13]. Sawada et al. reported the existence of these precipitates in the extracted residue of the grip portion of PiHA ruptured after 5319.3 h at 1173 K [13]. While a dynamical simulation technique of the EBSP has been established, a kinematical simulation was applied to the precipitates to reduce the calculation costs of the complex crystal structure. The difference in the simulated master patterns of the five phases permits us to distinguish the phases via Spherical Indexing.

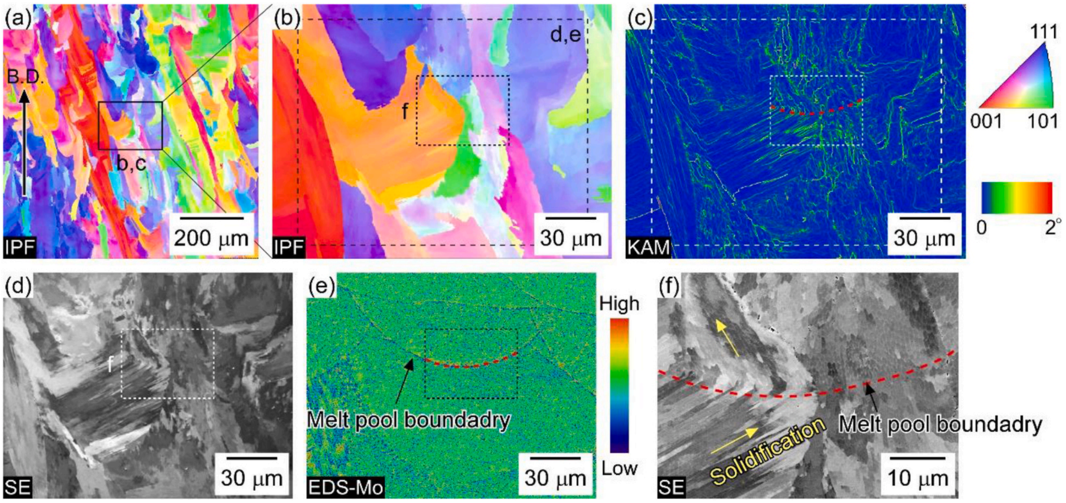

Fig. 1. (a)(b) Inverse pole figure (IPF) maps, (c) Kernel average misorientation (KAM) map obtained by SEM-EBSD, (d)(f) Secondary electron (SE) images and (e) Mo map obtained by SEM-EDS taken from as-built PiHA.

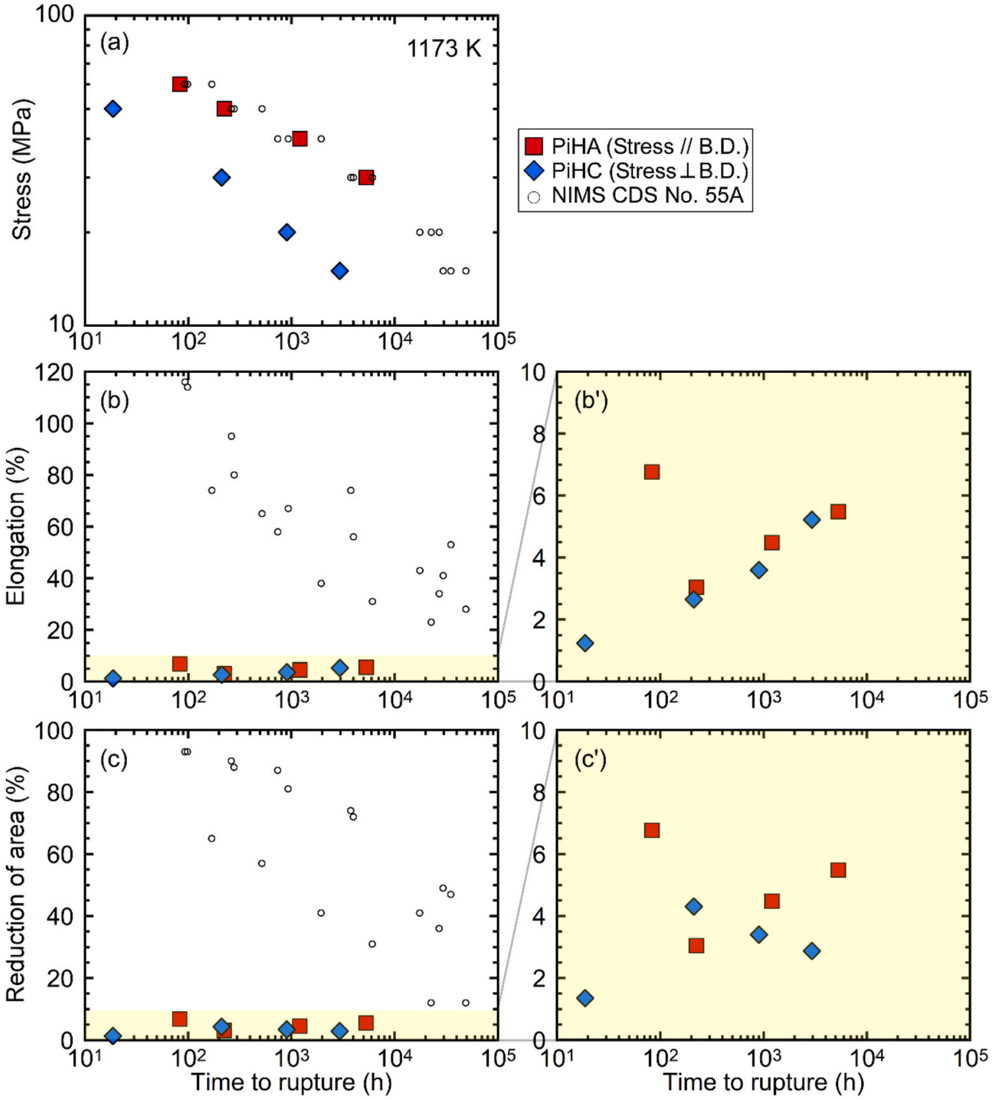

Fig. 2. (a) Stress vs. time to rupture, (b) elongation vs. time to rupture, and (c) reduction of area vs. time to rupture of the PiHA, PiHC, and conventional Hastelloy X [28,29] obtained by creep tests at 1173 K. (b') and (c') are the enlarged views of (b) and (c).

Phase	Ni	$M_{23}C_6$	R (Fe_3Mo_2)	M_6C	μ (Fe_7Mo_6)
Structure	Cubic	Cubic	Hexagonal	Cubic	Hexagonal
Space group	Fm-3m, 225	Fm-3m, 225	R-3, 148	Fd-3m, 227	R-3m, 166
Lattice parameter	a=0.356 nm	a=1.077 nm	a=1.098 nm c=1.948 nm	a=1.11 nm	a=0.477 nm c=2.577 nm
Simulation	Dynamical	Kinematical	Kinematical	Kinematical	Kinematical
Spherical Master pattern	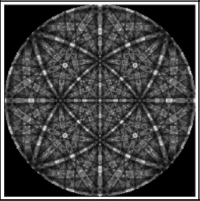	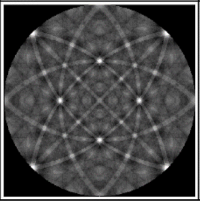	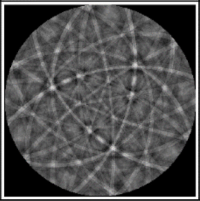	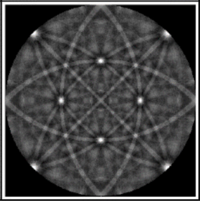	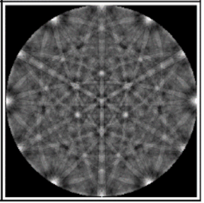

Fig. 3. Crystal structure, space group, lattice parameter and simulated spherical master patterns for Ni matrix and identified precipitates in extracted residue by Sawada et al. [13].

Fig. 4(a) shows the SE image of creep-ruptured PiHA. Creep voids and precipitates can be recognized as having darker and brighter contrasts, respectively. Fig. 4(b) shows the phase map obtained by EBSD reindexed by Spherical Indexing with a step size of 150 nm taken from the same area of Fig. 4(a). Precipitates recognized in the SE image were successfully indexed as $M_{23}C_6$, R, μ, and M_6C phases by Spherical

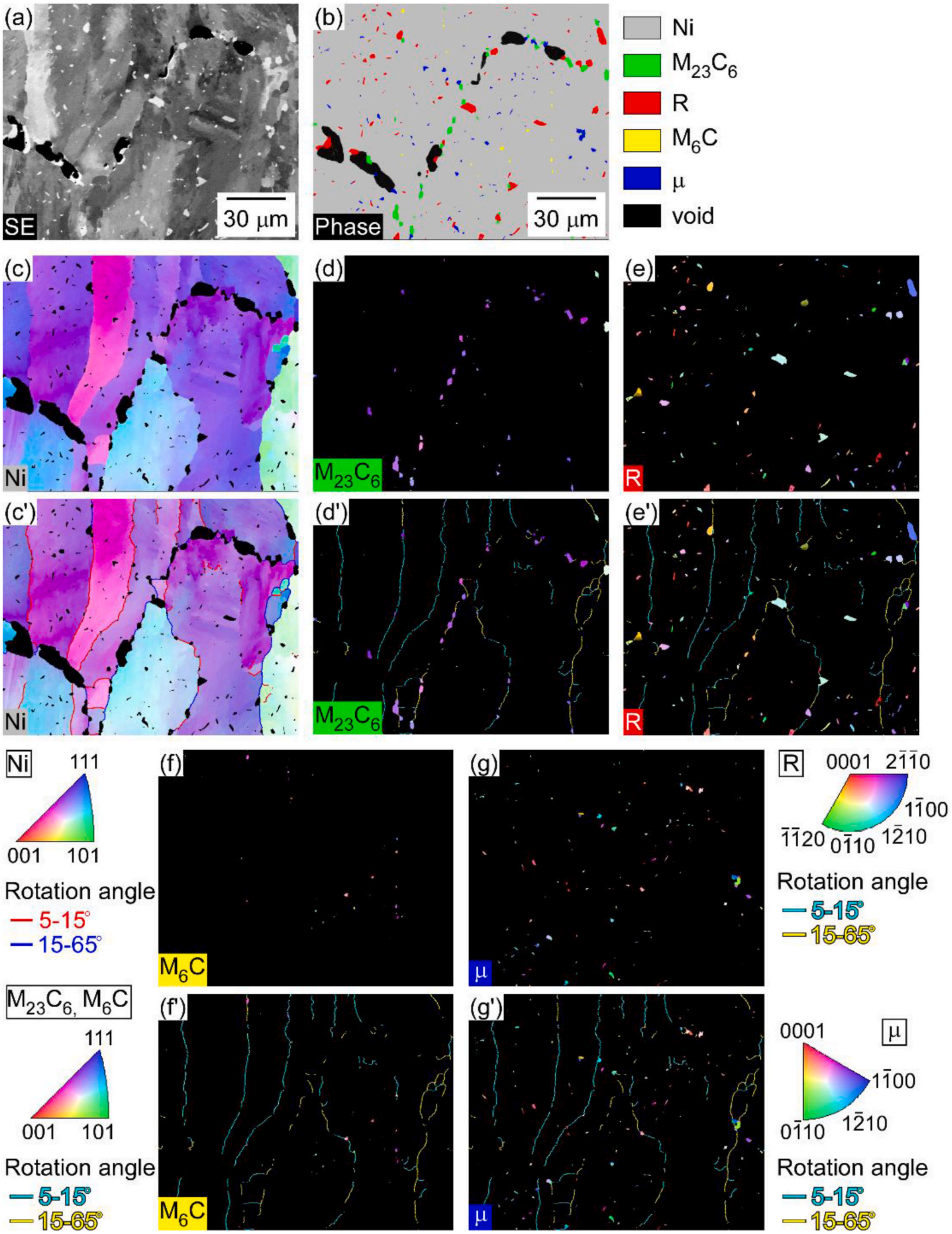

Fig. 4. (a) SE image, (b) phase map, IPF map for (c) Ni, (d) $M_{23}C_6$, (e) R, (f) M_6C, and (g) µ phases, IPF map for (c') Ni, (d') $M_{23}C_6$, (e') R, (f') M_6C, and (g') µ phases overlaid on low angle (5–15°) and high angle (>15°) grain boundaries of Ni identified by Spherical indexing of EBSD patterns of PiHA creep-ruptured after 5319.3 h at 1173 K under 30 MPa.

Table 4
Major precipitation sites of the $M_{23}C_6$, R, M_6C, and µ phases.

Phase	GI	LAGB (5-15 deg.)	HAGB (>15 deg.)
$M_{23}C_6$			●
R	●		●
M_6C	●	●	
µ	●	●	●

Indexing. The pixels with poor image quality (IQ) values less than the threshold are assumed to be voids. It was revealed that the creep voids were preferentially located on the precipitates. This was attributed to strain accumulation in the vicinity of the precipitates [30].

Fig. 4(c)–(g) are IPF maps of the Ni matrix, $M_{23}C_6$, R, µ, and M_6C phases. Low-angle (rotation angle: 5–15°) and high-angle (>15°) grain boundaries of the Ni matrix are also drawn for reference in Fig. 4(c')–(g'). From these images, the major precipitation sites of the precipitates were evaluated and classified into grain interior (GI), low-angle grain boundary (LAGB), and high-angle grain boundary (HAGB), as summarized in Table 4. Notably, as can be seen in Fig. 4(f) and (g), M_6C is agglomerated on the lower right side of the image, and the precipitated region has fewer µ phases. This suggests that segregation of Mo along the melt pool boundaries, as revealed in Fig. 1(e), influences the precipitation behavior of the M_6C and μ phases.

Fig. 5(a) shows the phase map of creep-ruptured PiHA, which is an enlarged view of the bottom-left region of Fig. 4(b). Fig. 5(b) and (c) present the IPF maps of Ni matrix and $M_{23}C_6$, respectively, for the same area as in Fig. 5(a). The EBSP acquired from grain A, grain B, and $M_{23}C_6$-A, as defined in Fig. 5(a)–(c), are shown in Fig. 5(d), (e), and (f), respectively. As shown in Fig. 3, both the Ni matrix and $M_{23}C_6$ phase exhibit the same crystal structure (Fm-3m). The bands generated by diffraction on the (111) plane of the Ni matrix and $M_{23}C_6$ are indicated by dashed lines. Because the band positions of the EBSPs obtained from grain B and $M_{23}C_6$-A are identical, it is suggested that $M_{23}C_6$-A has a cube-on-cube orientation relationship with grain B, whereas there is no orientation relationship with grain A [20,31].

Fig. 5(g) shows the pole figure for the (111) plane of grains A, B, and $M_{23}C_6$-A. The orientations of grain B and $M_{23}C_6$-A were in good agreement, consistent with a cube-on-cube orientation relationship, whereas no orientation relationship was observed between grain A and $M_{23}C_6$-A. Fig. 5(h) presents the SE image taken around $M_{23}C_6$-A. The pole figures shown in Fig. 5(g) suggest that the interface between grain B and $M_{23}C_6$-A exhibits an orientation relationship of $(111)_{Ni}//(111)_{M23C6}$. In other words, creep voids were preferentially formed at the interface between grain A and $M_{23}C_6$-A, where there was no orientation relationship, as reported in austenitic steels [20]. Please note that no definitive orientation relationship between the Ni matrix and other precipitates was identified based on the EBSD data obtained in this study.

To confirm the accuracy of the phase identification by EBSD and Spherical Indexing, SEM-EDS analysis was performed for creep-ruptured PiHA on the same area of Fig. 4. Fig. 6 shows (a) SE image and (b) C (c) Cr, (d) Mo, (e) Fe, and (f) Ni maps obtained by SEM-EDS. Please note that to avoid the effect of contamination attached during EBSD, the surface was re-polished by colloidal silica for 5 min. Therefore, the distribution of the tiny precipitates does not entirely match the EBSD results shown in Fig. 4.

As indicated in Fig. 6(b), the carbon concentration in the vicinity of the voids was enhanced. This was considered contamination that was not removed by polishing and subsequent ultrasonic cleaning. The Cr map (Fig. 6(c)) and Mo map (Fig. 6(d)) revealed the existence of Cr-rich and Mo-rich precipitates. Nevertheless, further distinguishing the Mo-rich precipitates into R, μ, and M_6C was difficult solely from the map.

Scatter diagram analysis is effective for classifying multiple phases with similar chemical composition [32–34]. Fig. 7(a)–(f) shows the scatter diagram of the characteristic X-ray intensities of Mo-L, Fe-K, Cr-K, and C-K obtained from the maps in Fig. 6. The region with the highest plot density is the Ni matrix. Fig. 7(g) shows an enlarged view of the scatter diagram of Mo-L vs. Cr-K. As highlighted in black, the Mo-poor data points are voids. The plot cluster extended to the Cr- and Mo-rich side, highlighted in green in Fig. 7(g), is considered as $M_{23}C_6$. In addition, there is another plot cluster extended to the Mo-rich side. The cluster had two enriched regions at the tip, suggesting the existence of (at least) two types of precipitates. Slightly Cr-rich and Cr-poor phases are suggested to be R and μ phases, respectively. The carbon-enriched region, highlighted in yellow in Fig. 7(g), is the contamination vicinity of the voids.

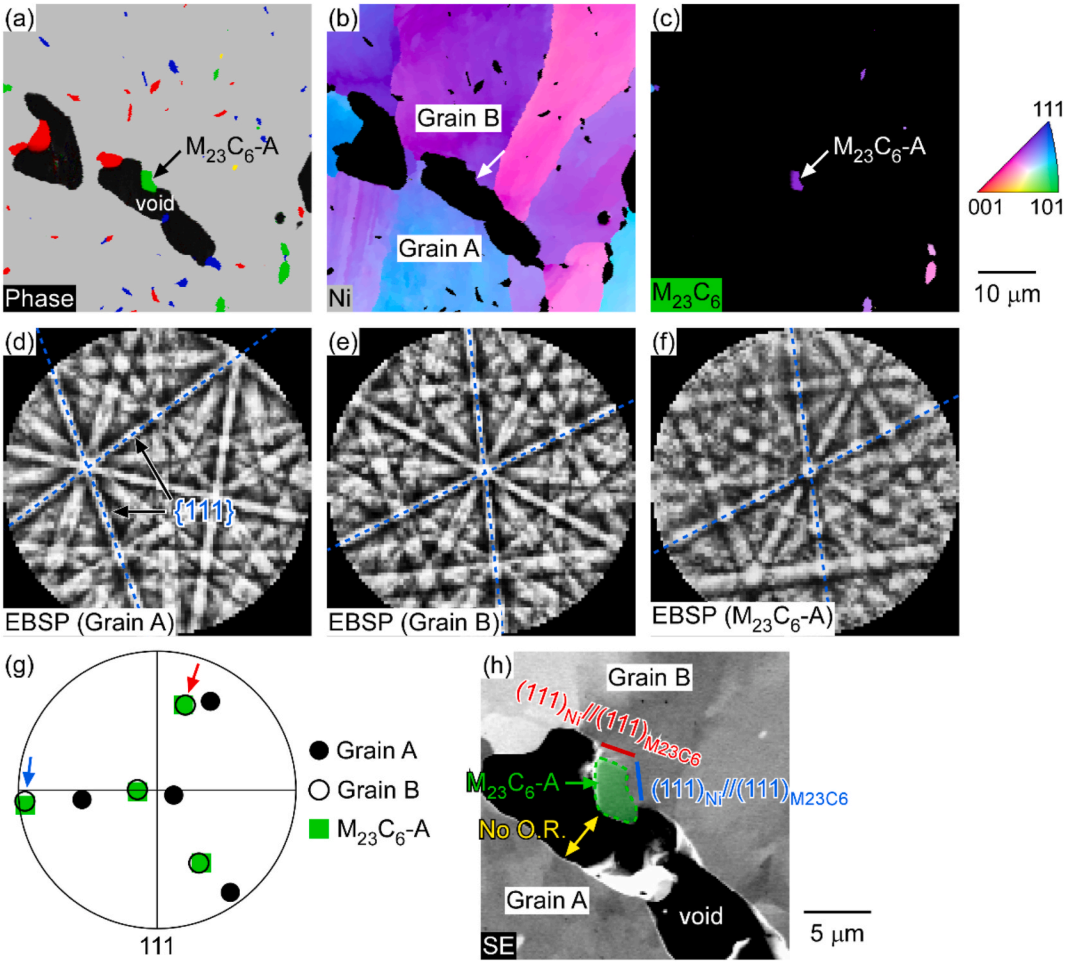

Fig. 5. Enlarged view of (a) phase map, IPF map of (b) Ni, and (c) $M_{23}C_6$ of those shown in Fig. 4. EBSD pattern taken from (d) grain A, (e) grain B in (b) and (f) $M_{23}C_6$-A in (c). (g) Pole figure of grains A, B, and $M_{23}C_6$-A and (h) SE image of PiHA creep-ruptured after 5319.3 h at 1173 K under 30 MPa.

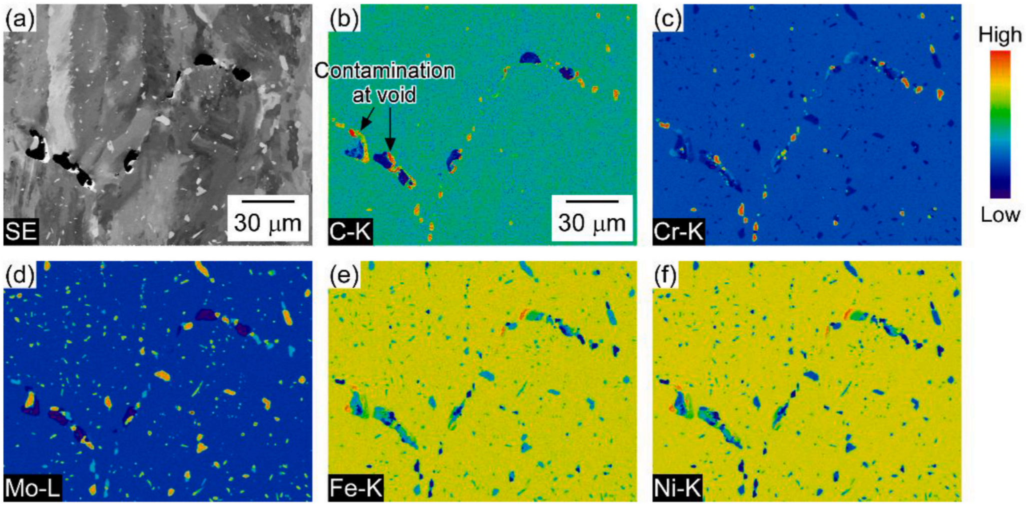

Fig. 6. (a) SE image, (b) C (c) Cr, (d) Mo, (e) Fe, and (f) Ni maps obtained by SEM-EDS taken from PiHA creep-ruptured after 5319.3 h at 1173 K under 30 MPa.

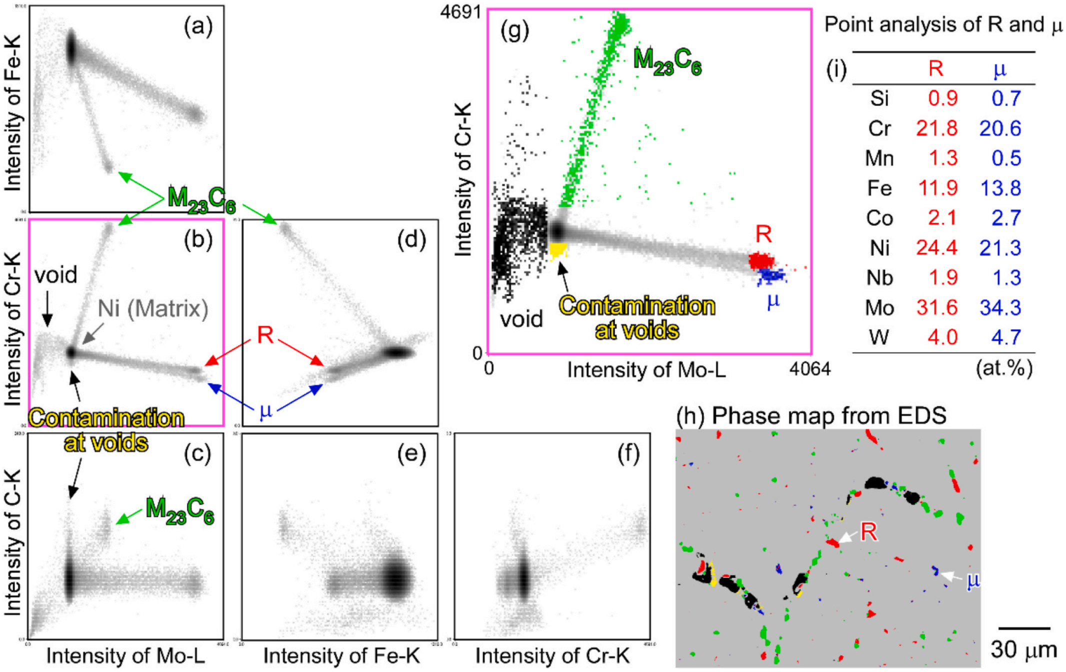

Point analysis of R and μ

(i)

	R	μ
Si	0.9	0.7
Cr	21.8	20.6
Mn	1.3	0.5
Fe	11.9	13.8
Co	2.1	2.7
Ni	24.4	21.3
Nb	1.9	1.3
Mo	31.6	34.3
W	4.0	4.7

(at.%)

Fig. 7. Scatter diagram of the characteristic X-ray intensity of (a) Mo-L vs Fe-K, (b) Mo-L vs Cr-K, (c) Mo-L vs C-K, (d) Fe-K vs Cr-K, (e) Fe-K vs C-K, and (f) Cr-K vs C-K. (g) Enlarged view of (b) with color for regions identified as precipitates, voids, and contamination. (h) Phase map converted from (g). (i) Chemical composition of R and μ phases obtained from the point analysis of these phases indicated in (h). (For interpretation of the references to color in this figure legend, the reader is referred to the Web version of this article.)

The plots with colors identified as precipitates were converted to the x-y coordinates as the phase map in Fig. 7(h). The distribution behavior of the relatively coarse $M_{23}C_6$, R, and μ phases showed good agreement with that obtained via EBSD (Fig. 4(b)). Therefore, the reliability of EBSD-based phase classification with Spherical Indexing was confirmed. However, the small R and μ phases in the grain interior, which correspond to the plots between the Ni matrix and R/μ phases in Fig. 7(g), could not be clustered because of their minor difference in the scatter diagram. Furthermore, the M_6C phase could not be identified via the scatter diagram of the EDS map because its size was much smaller than the interaction volume of the characteristic X-rays. In other words, EBSD was advantageous for analyzing smaller precipitates in terms of the smaller interaction volume of the signal. Fig. 6(i) shows the chemical compositions of the R and μ phases obtained from the point analysis of the precipitates indicated by arrows in Fig. 7(h). This revealed that the μ phase is slightly richer in Mo than the R phase.

Fig. 8(a) and (b) show the EBSD-based phase maps of creep-ruptured PiHA and PiHC, respectively. EBSD was performed with a step size of 1 μm; indexing of precipitates with a size much less than 1 μm was not successful. As previously reported, zigzag and straight crack propagation were observed in PiHA and PiHC, respectively.

Fig. 9 shows the relationship between the number density of the four types of precipitates and the frequency of precipitates observed on voids (= number of precipitates observed on voids/number of voids) for creep-ruptured PiHA and PiHC. This was evaluated from the EBSD-based phase map in Fig. 7(a) and (b). As the step size of the EBSD map was 1 μm, the precipitate, which was much smaller than the step size, was not evaluated. Fig. 9 reveals that the number density of precipitates and the

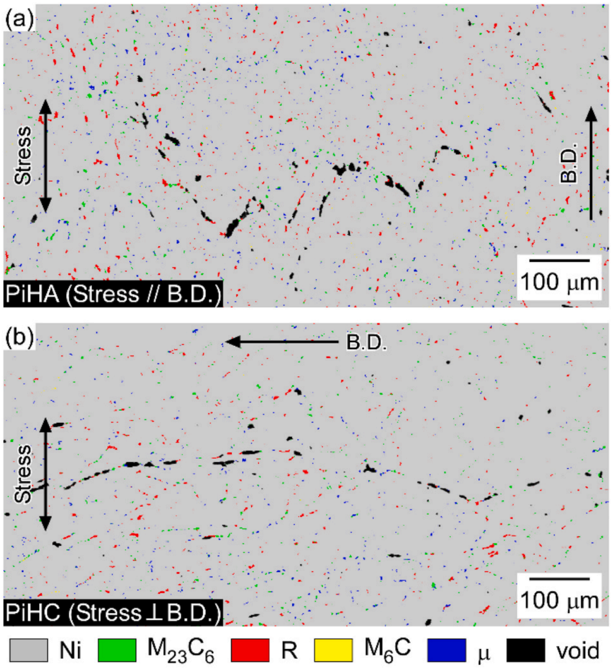

Fig. 8. EBSD-based Phase maps of (a) PiHA creep-ruptured after 5319.3 h at 1173 K under 30 MPa and (b) PiHC creep-ruptured after 2949.5 h at 1173 K under 15 MPa.

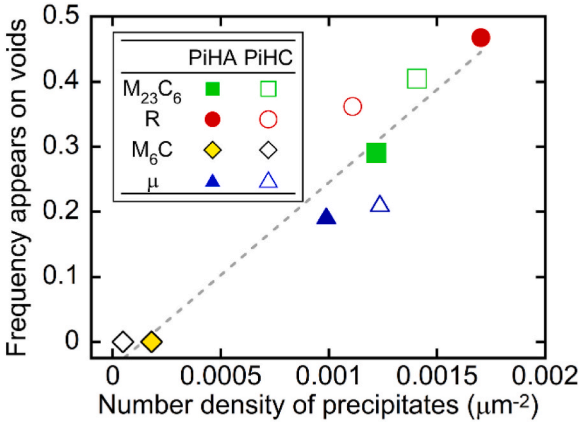

Fig. 9. Relationship between number density of precipitates and frequency of precipitates appearing in voids.

frequency of precipitates observed on voids have linear relationships. Therefore, it was suggested that there were no specific precipitates that preferentially contributed to creep void formation. In other words, the precipitation behavior contributes less to creep strength anisotropy.

3.3. *Grain boundary characterization of creep-ruptured samples*

Fig. 10(a) and (b) show the IPF map of the Ni matrix overlaid on the IQ map of all data of creep-ruptured PiHA and PiHC, respectively. Black pixels represent creep voids and cracks, where they have poor IQ values. Creep voids and cracks were formed on the grain boundaries.

Fig. 11(a) shows the frequency of the grain boundary misorientation angle of the as-built PiHA and the frequency of creep voids and cracks for each grain boundary misorientation angle bin (= number of grain boundaries in the misorientation angle bin with voids or cracks/number of grain boundaries with voids or cracks) in creep-ruptured PiHA and PiHC. The former value was obtained by analyzing the length of the grain boundaries using the EBSD map data shown in Fig. 1(a), and the latter values were obtained by measuring misorientation angles of approximately 40 grain-pairs sandwiching voids or cracks appearing in Fig. 10. It was revealed that while the frequency of LAGB with a misorientation angle of 5–15° was the highest, cracks frequently formed at HAGB with a misorientation angle of >15°. The trend in the crack frequency was slightly different between PiHA and PiHC. In other words, the voids and crack densities were remarkable in the misorientation angles of 25–45° for PiHA and 25–55° for PiHC in the observed area. It was considered that this difference was attributed to the relationship between the texture and the stress direction.

Fig. 11(b) shows the relationship between the grain boundary frequency of the as-built sample and the crack frequency of creep-ruptured PiHA and PiHC. This clearly revealed the preferential formation of voids and cracks at the HAGB and the higher void and crack formation resistance of the LAGB. This can be explained by the higher grain boundary energy [35] and susceptibility to grain boundary sliding [36] of HAGB compared to those of LAGB.

Fig. 12(a) and (b) show the LAGB and HAGB maps of the Ni matrix of creep-ruptured PiHA and PiHC, respectively. It was confirmed that zigzag cracks (PiHA) and straight cracks (PiHC) preferentially propagated at the HAGB perpendicular to the stress direction.

Fig. 13(a) shows the LAGB and HAGB maps of the as-built PiHA. The HAGB in Fig. 13(a), in which the rotation angle is greater than 15°, is shown in Fig. 13(b). To investigate the anisotropy of the HAGB distribution, a fast Fourier transform (FFT) was performed for Fig. 13(b), and the result is shown in Fig. 13(c). Please note that the contrast and color of the FFT-processed image have been optimized for better visibility. The region with high intensity was extended horizontally. This indicates that the HAGB is preferentially elongated along the building direction. In other words, effective grain size of the PiHA is much larger than that of the PiHC. This would be one of the reasons for the anisotropic creep strength.

Because creep voids preferentially form HAGB perpendicular to the stress direction, the anisotropy of the grain boundary distribution could affect creep behavior. In PiHA, there were fewer grain boundaries perpendicular to the stress direction. This results in zigzag crack

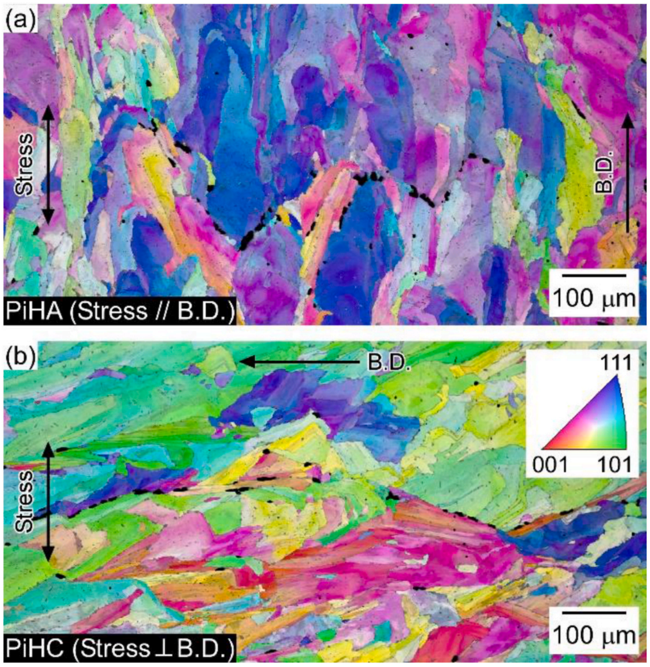

Fig. 10. IQ map of all data + IPF maps of Ni matrix of (a) PiHA creep-ruptured after 5319.3 h at 1173 K under 30 MPa and (b) PiHC creep-ruptured after 2949.5 h at 1173 K under 15 MPa.

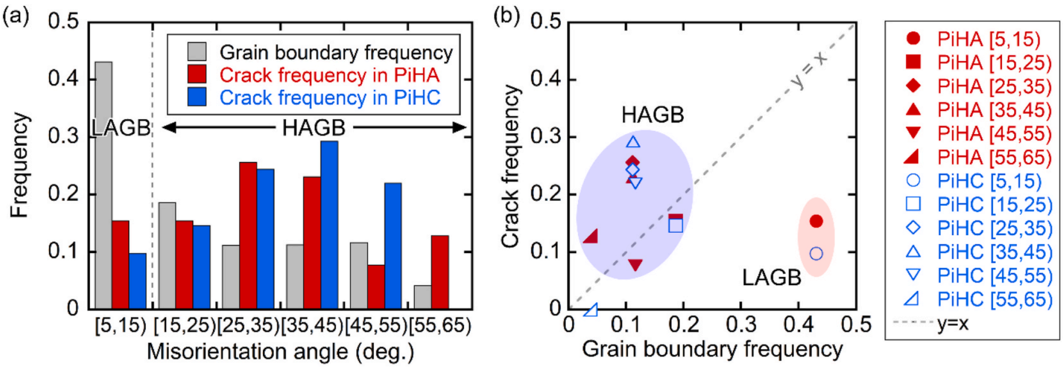

Fig. 11. (a) Frequency of the grain boundary and crack in PiHA creep-ruptured after 5319.3 h at 1173 K under 30 MPa and PiHC creep-ruptured after 2949.5 h at 1173 K under 15 MPa vs misorientation angle of grain boundary. (b) Relationship between grain boundary frequency and crack frequency in creep-ruptured PiHA and PiHC.

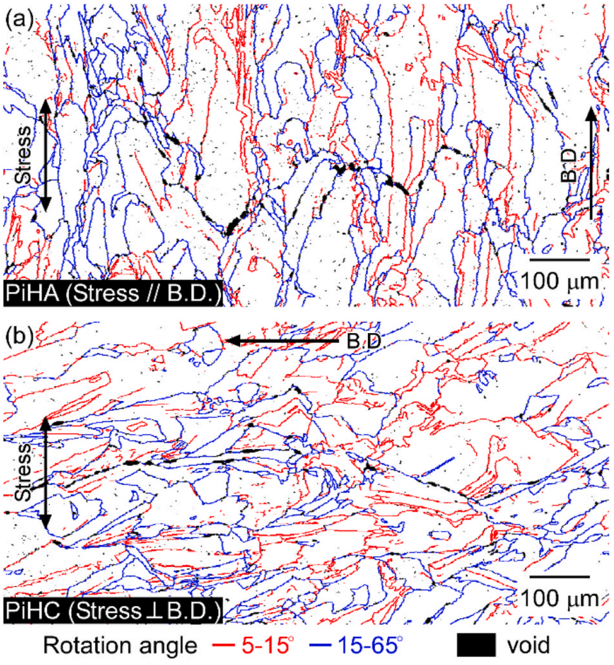

Fig. 12. Grain boundary maps of Ni matrix of (a) PiHA creep-ruptured after 5319.3 h at 1173 K under 30 MPa and (b) PiHC creep-ruptured after 2949.5 h at 1173 K under 15 MPa.

propagation, which is advantageous for a better creep life. In contrast, in PiHC, most of the grain boundaries are aligned perpendicular to the stress direction. This permits crack propagation with minimum energy, resulting in a lower creep strength. In other words, the anisotropy of the creep strength of the as-built LPBF-processed Hastelloy X was attributed to the anisotropic distribution of HAGB.

There are several intergranular creep fracture mechanisms, such as wedge cracks (w-type) and cavitation (r-type) [37]. Wedge cracks typically occur at the triple junction of grain boundaries, whereas cavitation occurs at the grain boundaries perpendicular to the stress direction. The voids and cracks observed in the creep-ruptured PiHA and PiHC were considered cavitation. The number density of grain boundary cavitation increases with creep strain [37]. Therefore, it was suggested that the preferential cavitation at the HAGB perpendicular to the stress direction was explained by localized creep deformation. Nevertheless, as shown in Fig. 12, there were HAGB perpendicular to the stress direction without voids and cracks. This heterogeneous cavitation mechanism needs to be discussed.

Fig. 14(a) and (b) show the Taylor factor maps of the Ni matrix of the creep-ruptured PiHA and PiHC, respectively. The Taylor factor was determined by considering the slip system of {111}<1-10> in the fcc grains. There were no marked differences in the Taylor factor between the creep-ruptured PiHA and PiHC. Fig. 14 reveals that creep voids and cracks were predominantly formed at the grain boundaries, where there was a significant deviation in the Taylor factor between adjacent grains. Therefore, the different deformability of adjacent grains owing to the Taylor factor mismatch enhanced the localized creep deformation, resulting in the preferential formation of creep voids and cracks on the HAGB [38].

4. Conclusions

The effect of building direction on the creep strength of LPBF-processed as-built Hastelloy X was investigated at 1173 K for up to several thousand hours. The creep rupture time was one order of magnitude shorter when the stress direction was perpendicular to the building direction than when it was parallel to the building direction.

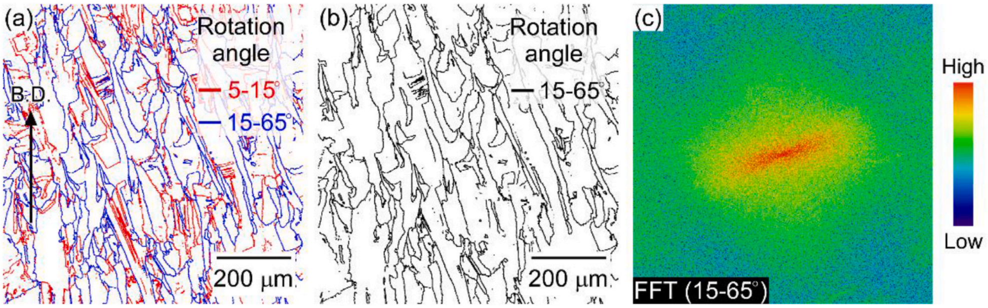

Fig. 13. (a) Grain boundary map with rotation angle of 5–15° and >15° of as-built PiHA, (b) Grain boundary map with rotation angle of >15°, and (c) fast Fourier transform (FFT) of (b).

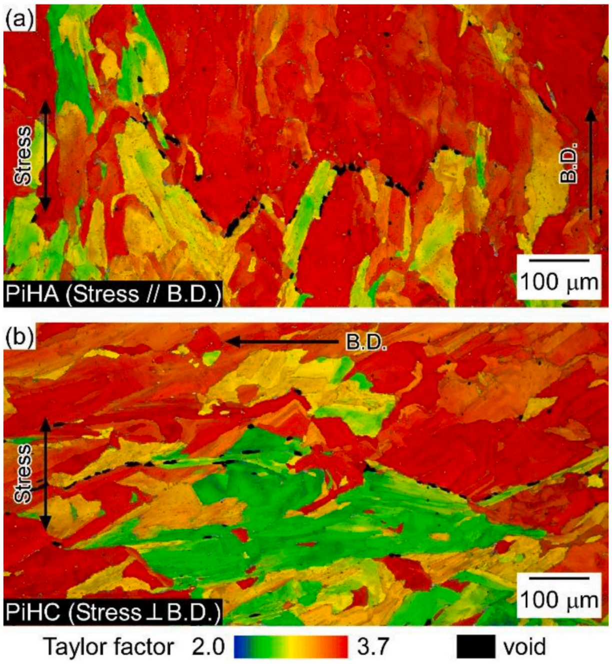

Fig. 14. Taylor factor maps of Ni matrix of (a) PiHA creep-ruptured after 5319.3 h at 1173 K under 30 MPa and (b) PiHC creep-ruptured after 2949.5 h at 1173 K under 15 MPa.

The origin of this strong anisotropy in creep strength was investigated in terms of precipitation behavior and grain boundary characteristics. The wide-area distributions of four precipitate phases—$M_{23}C_6$, R, μ, and M_6C—in creep-ruptured specimens were efficiently elucidated using SEM-EBSD combined with Spherical Indexing. However, specific precipitate phases are unlikely to contribute significantly to anisotropy in creep strength. In contrast, creep voids were preferentially formed along the high-angle grain boundaries, where there was a significant deviation in the Taylor factor between adjacent grains and perpendicular to the stress axis. As the high-angle grain boundaries in the as-built sample predominantly aligned along the building direction, our results suggest that the anisotropy in creep strength is attributable to the anisotropic distribution of high-angle grain boundaries, resulting in reduced creep resistance when the stress direction is perpendicular to the building direction. This indicates that controlling of the grain boundary structure through LPBF process is expected to enhance creep strength and reduce the anisotropy of LPBF-processed Hastelloy X.

CRediT authorship contribution statement

Tomotaka Hatakeyama: Writing – original draft, Visualization, Investigation, Formal analysis, Data curation. **Kota Sawada:** Writing – review & editing, Resources, Project administration, Investigation, Data curation, Conceptualization. **Masahiro Kusano:** Writing – review & editing, Resources, Investigation. **Makoto Watanabe:** Writing – review & editing, Supervision, Resources, Funding acquisition.

Declaration of competing interest

The authors declare that they have no known competing financial interests or personal relationships that could have appeared to influence the work reported in this paper.

Acknowledgement

The authors thank Mr. Masaru Suzuki and Mr. Kenji Kasahara for their support with additive manufacturing, Mr. Taku Moronaga and Ms. Akiko Nakamura for their support with microstructure characterization, and Mr. Yasushi Taniuchi, Dr. Kaoru Sekido, and Mr. Takehiro Nojima for their support with creep testing (all at NIMS). This work was partly supported by JSPS KAKENHI (JP25K01536) and Amada Foundation (AF-2022201-A3).

Data availability

Data will be made available on request.

References

[1] T. Hatakeyama, K. Sawada, M. Suzuki, M. Watanabe, Microstructure development of modified 9Cr-1Mo steel during laser powder bed fusion and heat treatment, Addit. Manuf. 61 (2023) 103350, https://doi.org/10.1016/J.ADDMA.2022.103350.
[2] T. Hatakeyama, K. Sawada, M. Kusano, M. Watanabe, Significant creep-strength improvement in modified 9Cr-1Mo steel via microstructural control through laser powder bed fusion, Addit. Manuf. 93 (2024) 104445, https://doi.org/10.1016/j.addma.2024.104445.
[3] Y. Yoshioka, D. Saito, K. Fujiyama, N. Okabe, Effect of microstructure on creep resistance of hastelloy X, Tetsu-To-Hagane 80 (1994) 789–794, https://doi.org/10.2355/tetsutohagane1955.80.10_789.
[4] S. Wu, S.B. Dai, M. Heilmaier, H.Z. Peng, G.H. Zhang, S. Huang, X.J. Zhang, Y. Tian, Y.M. Zhu, A.J. Huang, The effect of carbides on the creep performance of Hastelloy X fabricated by laser powder bed fusion, Mater. Sci. Eng., A 875 (2023) 145116, https://doi.org/10.1016/j.msea.2023.145116.
[5] S. Agrawal, C. Kumar, G.S. Avadhani, M. Heilmaier, S. Suwas, Anisotropic creep and stress rupture behaviour of laser powder bed fusion processed Hastelloy X, Mater. Sci. Eng., A 934 (2025) 148342, https://doi.org/10.1016/j.msea.2025.148342.
[6] Z. Huang, Z. Zhai, W. Lin, H. Chang, Y. Wu, R. Yang, Z. Zhang, On the orientation dependent microstructure and mechanical behavior of Hastelloy X superalloy fabricated by laser powder bed fusion, Mater. Sci. Eng. 844 (2022) 143208, https://doi.org/10.1016/j.msea.2022.143208.
[7] J. Kangazian, M. Shamanian, A. Kermanpur, E. Foroozmehr, M. Badrossamay, Investigation of microstructure-tensile behavior relationship in Hastelloy X Ni-based superalloy processed by laser powder-bed fusion: insights into the elevated temperature ductility loss, Mater. Sci. Eng., A 823 (2021) 141742, https://doi.org/10.1016/j.msea.2021.141742.
[8] S. Hibino, T. Todo, T. Ishimoto, O. Gokcekaya, Y. Koizumi, K. Igashira, T. Nakano, Control of crystallographic texture and mechanical properties of hastelloy-X via laser powder bed fusion, Crystals 11 (2021) 1–12, https://doi.org/10.3390/cryst11091064.
[9] A. Shaji Karapuzha, D. Fraser, D. Schliephake, S. Dietrich, Y. Zhu, X. Wu, A. Huang, Room and elevated temperature tensile and fatigue behaviour of additively manufactured Hastelloy X, Mater. Sci. Eng., A 882 (2023) 145479, https://doi.org/10.1016/j.msea.2023.145479.
[10] C.-H. Yu, R.L. Peng, T.L. Lee, V. Luzin, J.-E. Lundgren, J. Moverare, Anisotropic behaviours of LPBF Hastelloy X under slow strain rate tensile testing at elevated temperature, Mater. Sci. Eng., A 844 (2022) 143174, https://doi.org/10.1016/j.msea.2022.143174.
[11] S. Agrawal, G.S. Avadhani, S. Suwas, Deformation behaviour of additively manufactured Hastelloy X at high temperatures: the role of concurrent carbide precipitation, J. Alloys Compd. 1021 (2025) 179636, https://doi.org/10.1016/j.jallcom.2025.179636.
[12] S. Agrawal, G.S. Avadhani, S. Suwas, Evolution of new topologically close-packed phases P and R upon long-term isothermal aging of laser powder bed fusion processed Hastelloy X, J. Alloys Compd. 1010 (2025) 177597, https://doi.org/10.1016/j.jallcom.2024.177597.
[13] K. Sawada, T. Hatakeyama, M. Kusano, M. Watanabe, Creep data of Hastelloy X fabricated by laser powder bed fusion, Sci. Technol. Adv. Mater.: Methods 5 (2025) 2582996, https://doi.org/10.1080/27660400.2025.2582996.
[14] J.-C. Zhao, M. Larsen, V. Ravikumar, Phase precipitation and time–temperature-transformation diagram of Hastelloy X, Mater. Sci. Eng., A 293 (2000) 112–119, https://doi.org/10.1016/S0921-5093(00)01049-2.
[15] N.C. Krieger Lassen, D. Juul Jensen, K. Conradsen, Image processing procedures for analysis of electron back scattering patterns, Scanning Microsc. 6 (1992) 115–121.
[16] S.I. Wright, B.L. Adams, Automatic analysis of electron backscatter diffraction patterns, Metall. Trans. A 23 (1992) 759–767, https://doi.org/10.1007/BF02675553.
[17] W.C. Lenthe, S. Singh, M. De Graef, A spherical harmonic transform approach to the indexing of electron back-scattered diffraction patterns, Ultramicroscopy 207 (2019) 112841, https://doi.org/10.1016/j.ultramic.2019.112841.
[18] R. Hielscher, F. Bartel, T.B. Britton, Gazing at crystal balls: Electron backscatter diffraction pattern analysis and cross correlation on the sphere, Ultramicroscopy 207 (2019) 112836, https://doi.org/10.1016/j.ultramic.2019.112836.
[19] S.F. Bordín, S. Limandri, J.M. Ranalli, G. Castellano, EBSD spatial resolution for detecting sigma phase in steels, Ultramicroscopy 171 (2016) 177–185, https://doi.org/10.1016/j.ultramic.2016.09.010.
[20] T. Hatakeyama, K. Sawada, K. Sekido, K. Kimura, Beneficial role of the grain boundary precipitates for intergranular creep fracture of 25Cr–20Ni–Nb–N steel,

Mater. Sci. Eng., A 882 (2023) 145487, https://doi.org/10.1016/j.msea.2023.145487.

[21] Japanese industrial standards (JIS), Method of creep and creep rupture test for metallic materials, JIS Z 2271 (1998).

[22] M. Kusano, T. Osada, M. Watanabe, Data-driven optimization of laser scanning conditions in laser powder bed fusion for defect-free IN738LC components, J. Manuf. Process. 151 (2025) 354–371, https://doi.org/10.1016/j.jmapro.2025.07.023.

[23] H. Gao, Z. Zhang, J. Li, J. Sun, H. Xiang, B. Wu, W. Li, Q. Wei, Enhancement of epitaxial growth and mechanical properties of DZ125 superalloy fabricated by defocused-laser powder bed fusion via rotation angle optimization, Mater. Sci. Eng., A 930 (2025) 148113, https://doi.org/10.1016/j.msea.2025.148113.

[24] T. Hatakeyama, K. Sawada, Effect of lattice parameters of master pattern on EBSD indexing via pattern matching, J. Japan Inst.Met.Mater. 90 (2026).

[25] T. Hatakeyama, K. Sawada, Creep damage evaluation of 18Cr–9Ni–3Cu–Nb–N steel by electron backscattered diffraction (EBSD) – comparison of traditional Hough indexing and novel spherical indexing, Micron 199 (2025) 103908, https://doi.org/10.1016/j.micron.2025.103908.

[26] F. Sun, T. Ogawa, Y. Adachi, K. Sato, S. Takagi, G. Miyamoto, A. Suzuki, A. Yamanaka, N. Nakada, T. Ishimoto, T. Nakano, Y. Koizumi, Modulated structure formation in dislocation cells in 316L stainless steel fabricated by laser powder bed fusion, Mater. Trans. 64 (2023), https://doi.org/10.2320/matertrans.MT-ME2022004. MT-ME2022004.

[27] D.E. Jodi, T. Kitashima, M. Watanabe, Effect of scan strategy on the formation of a pure nickel single-crystal structure using a flat-top laser beam via laser powder bed fusion, Sci. Technol. Adv. Mater. 24 (2023), https://doi.org/10.1080/14686996.2023.2201380.

[28] NIMS Creep Data Sheet, No. 55A, National Institute for Materials Science, 2023.

[29] K. Sawada, Y. Taniuchi, K. Sekido, T. Nojima, T. Hatakeyama, K. Kimura, Long-term creep properties of Ni-based 21Cr-18Fe-9Mo superalloys, Sci. Technol. Adv. Mater.: Methods 3 (2023), https://doi.org/10.1080/27660400.2023.2284129.

[30] G.B. Sarma, B. Radhakrishnan, Modeling the effect of microstructural features on the nucleation of creep cavities, Mater. Sci. Eng., A 494 (2008) 92–102, https://doi.org/10.1016/j.msea.2007.10.095.

[31] T. Hatakeyama, K. Sawada, Precipitation behavior of the M23C6 phase on the coherent twin boundary of 25Cr-20Ni-Nb-N steel, Mater. Lett. 363 (2024) 136277, https://doi.org/10.1016/j.matlet.2024.136277.

[32] T. Kimura, T. Sugizaki, K. Nishida, N. Ishikawa, S. Tanuma, Analysis of joining boundary between Ni-P electroless plate and solder by EPMA scatter diagram method (I), J. Jpn. Inst. Metals 68 (2004) 8–13, https://doi.org/10.2320/jinstmet.68.8.

[33] T. Hatakeyama, S. Ida, K. Sawada, K. Yoshimi, Microstructure development during creep deformation of 9Cr–1Mo–V–Nb steel with excess nitrogen introduced by solution nitriding – Multidimensional scatter diagram analysis of STEM-EDS maps by machine learning, Tetsu-To-Hagane 111 (2025), https://doi.org/10.2355/tetsutohagane.TETSU-2024-115. TETSU-2024-115.

[34] T. Hatakeyama, S. Ida, K. Sawada, K. Yoshimi, Microstructure development during creep deformation of 9Cr-1Mo-V-Nb steel with excess nitrogen introduced by solution nitriding – Multidimensional scatter diagram analysis of STEM-EDS maps by machine learning, ISIJ Int. (2025), https://doi.org/10.2355/isijinternational.ISIJINT-2025-211. ISIJINT-2025-211.

[35] W.T. Read, W. Shockley, Dislocation models of crystal grain boundaries, Phys. Rev. 78 (1950) 275–289, https://doi.org/10.1103/PhysRev.78.275.

[36] T. Watanabe, Grain boundary sliding and stress concentration during creep, Metall. Trans. A 14 (1983) 531–545, https://doi.org/10.1007/BF02643771.

[37] M.E. Kassner, T.A. Hayes, Creep cavitation in metals, Int. J. Plast. 19 (2003) 1715–1748, https://doi.org/10.1016/S0749-6419(02)00111-0.

[38] M. Masoumi, C.C. Silva, I.A. Lemos, L.F.G. Herculano, H.F.G. de Abreu, Role of crystallographic textures on failure behavior in HSLA Grade-420 steel during cold rolling, J. Mater. Eng. Perform. 26 (2017) 1531–1539, https://doi.org/10.1007/s11665-017-2577-y.